

Structural and Magnetic Phase Transitions in $\text{CeCu}_{6-x}\text{T}_x$ ($T = \text{Ag, Pd}$)

L. Poudel^{1,2}, C. de la Cruz², E. A. Payzant³, A. F. May⁴, M. Koehler⁵, V. O. Garlea², A. E. Taylor², D. S. Parker⁴, H. B. Cao², M. A. McGuire⁴, W. Tian², M. Matsuda², H. Jeon^{4,6}, H. N. Lee⁴, T. Hong², S. Calder², H. D. Zhou¹, M. D. Lumsden², V. Keppens⁵, D. Mandrus^{1,4,5} and A. D. Christianson^{1,2}

¹Department of Physics & Astronomy, University of Tennessee, Knoxville, TN-37966, USA

²Quantum Condensed Matter Division, Oak Ridge National Laboratory, Oak Ridge, TN-37831, USA

³Chemical & Engineering Materials Division, Oak Ridge National Laboratory, Oak Ridge, TN 37831, USA

⁴Materials Science & Technology Division, Oak Ridge National Laboratory, Oak Ridge, TN-37831, USA

⁵Department of Material Science & Engineering, University of Tennessee, Knoxville, TN-37966, USA

⁶Department of Physics, Pusan National University, Busan 609-735, Korea

(Dated: June 24, 2022)

The structural and the magnetic properties of $\text{CeCu}_{6-x}\text{Ag}_x$ ($0 \leq x \leq 0.85$) and $\text{CeCu}_{6-x}\text{Pd}_x$ ($0 \leq x \leq 0.4$) have been studied using neutron diffraction, resonant ultrasound spectroscopy (RUS), heat capacity, x-ray diffraction measurements and first principles calculations. The structural and magnetic phase diagrams of $\text{CeCu}_{6-x}\text{Ag}_x$ and $\text{CeCu}_{6-x}\text{Pd}_x$ as a function of Ag/Pd composition are reported. The end member, CeCu_6 , undergoes a structural phase transition from an orthorhombic ($Pnma$) to a monoclinic ($P2_1/c$) phase at 240 K. In $\text{CeCu}_{6-x}\text{Ag}_x$, the structural phase transition temperature (T_s) decreases linearly with Ag concentration and extrapolates to zero at $x_S \approx 0.1$. The structural transition in $\text{CeCu}_{6-x}\text{Pd}_x$ remains unperturbed with Pd substitution within the range of our study. The lattice constant b slightly decreases with Ag/Pd doping, whereas, a and c increase with an overall increase in the unit cell volume. Both systems, $\text{CeCu}_{6-x}\text{Ag}_x$ and $\text{CeCu}_{6-x}\text{Pd}_x$, exhibit a magnetic quantum critical point (QCP), at $x \approx 0.2$ and $x \approx 0.05$ respectively. Near the QCP, long range antiferromagnetic ordering takes place at an incommensurate wave vector ($\delta_1 \ 0 \ \delta_2$) where $\delta_1 \sim 0.62$, $\delta_2 \sim 0.25$, $x = 0.125$ for $\text{CeCu}_{6-x}\text{Pd}_x$ and $\delta_1 \sim 0.64$, $\delta_2 \sim 0.3$, $x = 0.3$ for $\text{CeCu}_{6-x}\text{Ag}_x$. The magnetic structure consists of an amplitude modulation of the Ce-moments which are aligned along the c -axis of the orthorhombic unit cell.

I. INTRODUCTION

Understanding the nature of a quantum critical point (QCP) remains one of the most topical questions in condensed matter physics. The conventional model of a metallic QCP proposed by Hertz, Millis, and Moriya (HMM) describes the nature of the critical phenomena within the confines of an instability of a spin-density-wave[1–3]. Many systems near a QCP are consistent with the description of the HMM model[4–6]. For example: divergence of the Grüneisen ratio is observed in CeNi_2Ge_2 with the exponent $x = 1$ [7]; the heat capacity in $\text{Ce}(\text{Ni}_{1-x}\text{Pd}_x)_2\text{Ge}_2$ and CeCu_2Si_2 diverges with the relation $\gamma = \gamma_0 - \alpha T^{1/2}$ [7–9]; the resistivity at the ferromagnetic QCP of $\text{Ni}_x\text{Pd}_{1-x}$ obeys power law relation $\rho = \rho_0 + \alpha T^{5/3}$ [10]. However, the HMM model is not sufficient to explain many properties observed in a number of systems near a QCP[11–16], and a substantial subset of these systems are interpreted as hosting a “Local QCP”[14–18], where the breakdown of the Kondo-screening leaves the local-moments free to form a magnetic ground state.

The well-known heavy fermion system $\text{CeCu}_{6-x}\text{Au}_x$ ($x \approx 0.1$) is often considered as a prototypical example of a local QCP[19–23]. The nature of the spin fluctuation spectrum of $\text{CeCu}_{5.9}\text{Au}_{0.1}$ is peculiar and is not consistent with the conventional theory that successfully describes several aspects of many Ce-based heavy fermion materials[19–23]. Inelastic neutron scattering measurements of $\text{CeCu}_{5.9}\text{Au}_{0.1}$ show that the imaginary part of

the dynamic susceptibility at the QCP exhibits an E/T scaling relation $\chi''(\mathbf{Q}, E) = T^{-\alpha} f(E/T)$ with an anomalous value of the scaling exponent $\alpha \approx 0.75$ [19, 21, 24, 25]. The scaling relation as well as the logarithmic divergence of C/T with temperature in $\text{CeCu}_{6-x}\text{Au}_x$ are in accord with the behavior expected for a local QCP.

While great attention has been given to the evolution of magnetic properties with Au doping into CeCu_6 , less attention has been paid to the evolution of the structural properties. The $\text{CeCu}_{6-x}\text{Au}_x$ system exhibits a structural phase transition from orthorhombic ($Pnma$) to monoclinic ($P2_1/c$) that can be tuned by pressure or chemical doping[26, 27]. Previous studies have reported different values of the structural transition temperature (T_s) for the end member, CeCu_6 , but are all within the range 168 K - 230 K[26–30]. In $\text{CeCu}_{6-x}\text{Au}_x$, T_s decreases linearly with Au concentration and the structural phase transition disappears beyond the critical concentration, $x_S \approx 0.14$, which is close to the magnetic QCP, $x_{\text{QCP}} \approx 0.1$ [26, 31]. Moreover, one study indicates that the structural transition disappears and magnetic order emerges at nearly the same point in the phase diagram, raising the possibility that a quantum multi-critical point at $x_{\text{QCP}}^S \approx 0.13$ is the origin of the unusual quantum critical behavior in $\text{CeCu}_{6-x}\text{Au}_x$ [27]. Consequently, further investigation of the influence of the structural phase transition on the unconventional nature of the QCP in $\text{CeCu}_{6-x}\text{Au}_x$ is of interest.

Doping CeCu_6 with transition metals other than Au offers the opportunity to explore the nature of the QCP in an expanded parameter space where the structural and

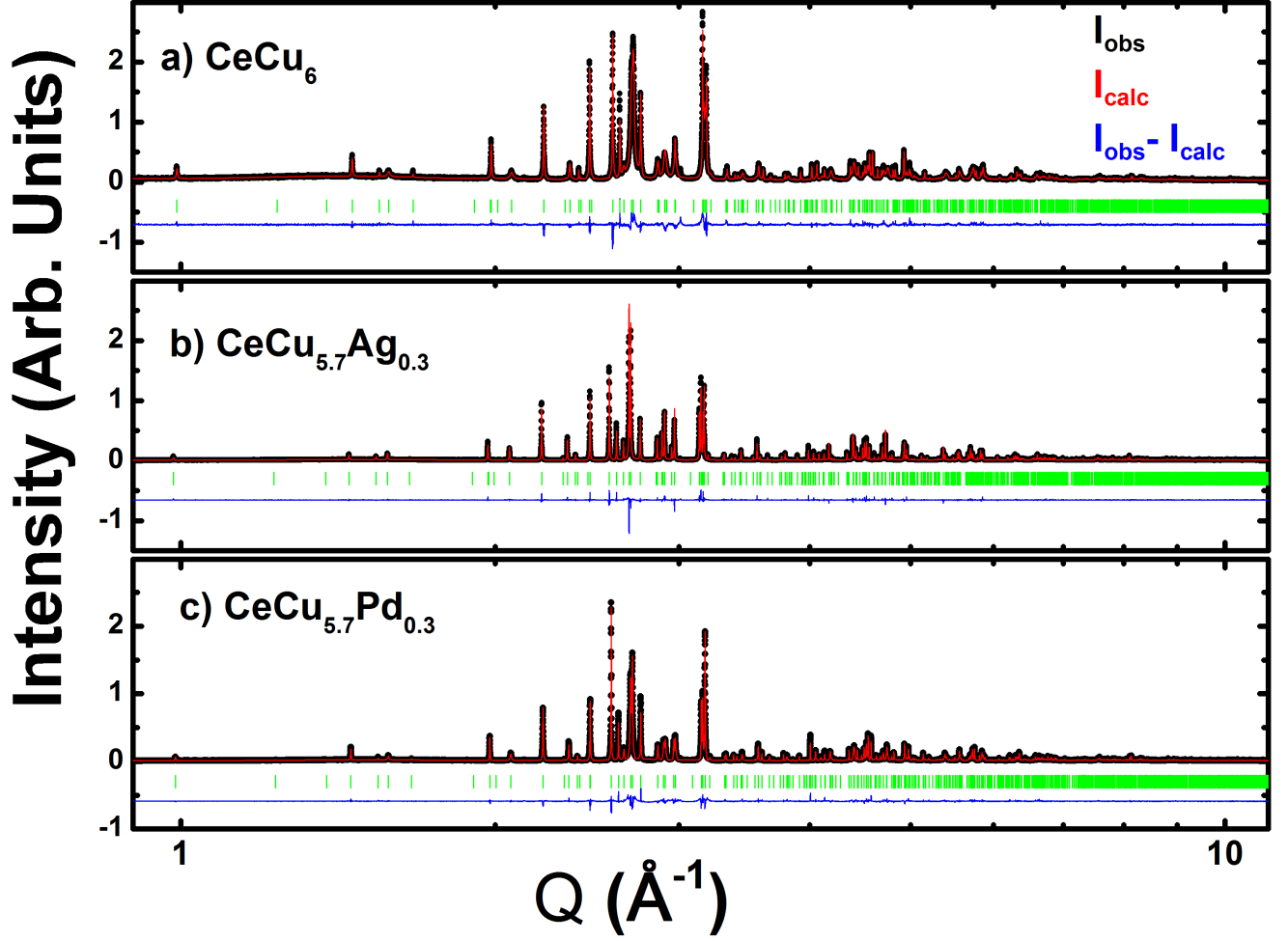


FIG. 1. (Color online) a) Room temperature x-ray powder diffraction pattern (black dots) plotted along with the Rietveld refinement (red line) for a) CeCu_6 , b) $\text{CeCu}_{5.7}\text{Ag}_{0.3}$ and c) $\text{CeCu}_{5.7}\text{Pd}_{0.3}$. Vertical green marks are the positions of the structural reflections. The diffraction patterns were collected at beamline 11-BM at the Advance Photon Source (APS) of Argonne National Laboratory (ANL). The values of the refined parameters are tabulated in tables I and II. The difference ($I_{\text{obs}} - I_{\text{calc}}$) is offset for clarity. Note: the x-axis (Q) is in a logarithmic scale.

magnetic degrees of freedom can potentially be decoupled. For example, $\text{CeCu}_{6-x}\text{Ag}_x$ [32–34], $\text{CeCu}_{6-x}\text{Pd}_x$ [35], $\text{CeCu}_{6-x}\text{Pt}_x$ [35] and $\text{CeCu}_{6-x}\text{Sn}_x$ [36] all exhibit an antiferromagnetic order that evolves with doping. In the Ag/Pt/Pd-doped systems, deviation from Fermi-liquid behavior is reported at the QCP[35, 37, 38]. Furthermore, in $\text{CeCu}_{6-x}\text{Ag}_x$, thermal expansion measurements indicate that the divergence of the Grüneisen ratio is much weaker than that expected from the HMM model suggesting that the critical behavior is unconventional[39].

In this paper, we present the first comprehensive neutron and x-ray diffraction investigation of the structural and magnetic properties of the $\text{CeCu}_{6-x}\text{Ag}_x$ and the $\text{CeCu}_{6-x}\text{Pd}_x$ systems. The structural properties were studied using neutron diffraction, resonant ultrasound spectroscopy (RUS), and x-ray diffraction measurements for different compositions of $\text{CeCu}_{6-x}\text{Ag}_x$ and

$\text{CeCu}_{6-x}\text{Pd}_x$. Elastic neutron scattering measurements were performed for several members of $\text{CeCu}_{6-x}\text{Ag}_x$ and $\text{CeCu}_{6-x}\text{Pd}_x$ to build a detailed understanding of the evolution of the antiferromagnetic phase with doping. The Neel temperatures (T_N) obtained from neutron diffraction measurements in both systems are in agreement with previously published work[35, 37]. In both systems, a continuous decrease in the ordered moment is observed as the QCP is approached. The values of T_s in $\text{CeCu}_{6-x}\text{Ag}_x$ decrease linearly with Ag-composition, until the structural phase transition disappears at the critical concentration, $x_S \approx 0.1$. In $\text{CeCu}_{6-x}\text{Pd}_x$, no change in the structural transition temperature is observed for $0 \leq x \leq 0.4$.

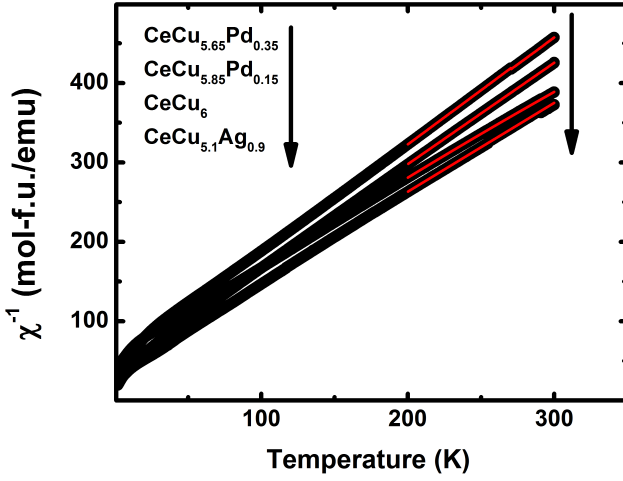


FIG. 2. (Color online) Inverse susceptibilities of $\text{CeCu}_{6-x}\text{T}_x$ ($\text{T} = \text{Ag}, \text{Pd}$) showing Curie-Weiss behavior. The red solid line is a Curie-Weiss fit to the data. The effective moments estimated from the Curie-Weiss fits are given in the text.

II. EXPERIMENTAL DETAILS

Single crystals and polycrystalline samples were synthesized for this study. Polycrystalline samples of $\text{CeCu}_{6-x}\text{T}_x$ ($\text{T} = \text{Ag}, \text{Pd}$) were synthesized by arc melting stoichiometric quantities of Ce (Ames laboratory, purity = 99.9999%), Cu (Alpha Aesar, purity = 99.9999%), Pd (Alpha Aesar, purity = 99.9999%) and Ag (Alpha Aesar, purity = 99.9999%) on a water-cooled copper crucible inside an ultra high purity argon atmosphere. The arc-melted buttons were flipped and remelted no less than four times to ensure homogeneity of the samples. Some samples were annealed at 750 °C for a week inside a silica tube back filled with argon. No change due to annealing was observed in the room temperature x-ray diffraction pattern or magnetization measurements. Single crystals of $\text{CeCu}_{6-x}\text{T}_x$ ($\text{T} = \text{Ag}, \text{Pd}$) were grown in a Tri-arc furnace using the Czochralski Technique. The growth was performed on a water-cooled copper hearth under an atmosphere of flowing ultra high purity argon. The crystals were pulled from the melt using a Tungsten seed rod rotating at ≈ 30 rev/minat with a speed of ≈ 20 mm/hr.

For analysis of the antiferromagnetic phase, neutron diffraction measurements were performed on several concentrations of $\text{CeCu}_{6-x}\text{Ag}_x$ (single crystals with $x = 0.3, 0.35, 0.4, 0.5, 0.75$ and polycrystalline samples with $x = 0.65, 0.85$) and $\text{CeCu}_{6-x}\text{Pd}_x$ (single crystals with $x = 0.125, 0.15$, and polycrystalline samples with $x = 0.25, 0.35, 0.4$). Approximately 10 g of polycrystalline sample was used for each measurement. The polycrystalline samples were ground inside a glove box and held inside a cylindrical aluminium container loaded in a ^3He refrigerator. The single crystal measurements were performed with ≈ 0.5 g samples. Each single crystal was pre-aligned using the neutron alignment station (CG-1B) at the High

TABLE I. Lattice parameters and atomic coordinates at room temperature of a) CeCu_6 , b) $\text{CeCu}_{5.7}\text{Ag}_{0.3}$ and c) $\text{CeCu}_{5.7}\text{Pd}_{0.3}$ obtained from Rietveld refinements of the structural model for the synchrotron x-ray measurements (See Fig. 1).

a) CeCu_6					
$R_p: 18.5 \quad R_{wp}: 21.0 \quad R_{exp}: 14.3 \quad \chi^2: 2.1$					
$a = 8.1105(1) \text{ \AA} \quad b = 5.1000(1) \text{ \AA} \quad c = 10.1622(2) \text{ \AA}$					
Atom	Wyck.	x/a	y/b	z/c	Occupancy
Ce	4c	0.2595(4)	0.2500	0.5646(4)	1
Cu1	8d	0.0639(5)	0.5085(12)	0.3075(6)	1
Cu2	4c	0.1469(8)	0.2500	0.8597(6)	1
Cu3	4c	0.3199(8)	0.2500	0.2522(5)	1
Cu4	4c	0.0604(10)	0.2500	0.0993(7)	1
Cu5	4c	0.4063(9)	0.2500	0.0134(7)	1

b) $\text{CeCu}_{5.7}\text{Ag}_{0.3}$					
$R_p: 14.2 \quad R_{wp}: 16.1 \quad R_{exp}: 9.43 \quad \chi^2: 2.93$					
$a = 8.1702(1) \text{ \AA} \quad b = 5.0979(1) \text{ \AA} \quad c = 10.2388(1) \text{ \AA}$					
Atom	Wyck.	x/a	y/b	z/c	Occupancy
Ce	4c	0.2605(5)	0.2500	0.5644(3)	1
Cu1	8d	0.0631(5)	0.5007(8)	0.3119(3)	1
Cu2	4c	0.1459(4)	0.2500	0.8593(3)	0.66(1)
Ag2	4c	0.1459(4)	0.2500	0.8593(3)	0.34(1)
Cu3	4c	0.3149(3)	0.2500	0.2512(3)	1
Cu4	4c	0.0608(4)	0.2500	0.1006(4)	1
Cu5	4c	0.4029(5)	0.2500	0.0146(4)	1

c) $\text{CeCu}_{5.7}\text{Pd}_{0.3}$					
$R_p: 15.9 \quad R_{wp}: 27.9 \quad R_{exp}: 9.4 \quad \chi^2: 4.82$					
$a = 8.13412(2) \text{ \AA} \quad b = 5.09530(1) \text{ \AA} \quad c = 10.19498(1) \text{ \AA}$					
Atom	Wyck.	x/a	y/b	z/c	Occupancy
Ce	4c	0.2605(5)	0.2500(0)	0.5648(3)	1
Cu1	8d	0.0641(6)	0.5062(15)	0.3093(6)	0.96(2)
Pd1	8d	0.0641(5)	0.5062(15)	0.3093(6)	0.04(2)
Cu2	4c	0.1443(8)	0.2500	0.8583(6)	0.80(2)
Pd2	4c	0.1443(8)	0.2500	0.8583(6)	0.20(2)
Cu3	4c	0.3167(9)	0.2500	0.2528(5)	1
Cu4	4c	0.0586(10)	0.2500	0.0980(8)	0.94(4)
Pd4	4c	0.0586(10)	0.2500	0.0980(8)	0.06(4)
Cu5	4c	0.4030(10)	0.2500	0.0158(7)	1

Flux Isotope Reactor (HFIR) of Oak Ridge National Laboratory (ORNL). All the samples were measured using the triple-axis spectrometers HB-1A, HB-1, HB-3, and CG-4C at HFIR (ORNL) using fixed incident and final energies of 14.7 meV (HB-1A), 13.5 meV (HB-1), 14.7 meV (HB-3), and 5 meV (CG-4C). A dilution refrigerator provided the sample environment for these measurements.

The structural phase transitions were characterized using RUS, x-ray, and neutron diffraction. High-resolution synchrotron x-ray diffraction patterns were obtained at room-temperature for CeCu_6 , $\text{CeCu}_{5.7}\text{Ag}_{0.3}$, and $\text{CeCu}_{5.7}\text{Pd}_{0.3}$ from 11-BM at Advance Photon Source (APS) of Argonne National Laboratory (ANL) using x-rays of incident wavelength, $\lambda \approx 0.41 \text{ \AA}$. X-ray diffraction patterns on polycrystalline samples of $\text{CeCu}_{6-x}\text{Ag}_x$ ($x = 0.015, 0.025, 0.065, 0.075$) and $\text{CeCu}_{6-x}\text{Pd}_x$ ($x = 0.025, 0.25, 0.3$) were collected using a PANalytical X'Pert Pro MPD powder diffractometer. Full patterns were collected at 300 K and 20 K, following

TABLE II. Structural parameters of $\text{CeCu}_{6-x}\text{T}_x$ ($T = \text{Ag, Pd}$) extracted from diffraction measurements at room temperature. The lattice parameters were obtained from Rietveld analysis.

	x	Measurement	a (Å)	b (Å)	c (Å)	Unit Cell Volume (Å ³)
CeCu ₆		x-ray	8.1105(1)	5.1010(1)	10.1622(2)	420.43(1)
	0.035	neutron	8.1215(9)	5.0976(6)	10.1775(8)	421.35(3)
CeCu _{6-x} Ag _x	0.1	neutron	8.1266(6)	5.0972(3)	10.1846(5)	421.87(2)
	0.3	x-ray	8.1702(1)	5.0979(1)	10.2388(1)	426.46(1)
	0.05	neutron	8.1103(6)	5.0998(4)	10.1649(3)	420.43(2)
CeCu _{6-x} Pd _x	0.1	neutron	8.1177(8)	5.0996(5)	10.1727(9)	421.11(3)
	0.3	x-ray	8.1341(2)	5.0953(1)	10.1950(1)	422.54(1)
	0.4	neutron	8.1444(8)	5.0899(4)	10.2042(8)	423.01(2)

which selected peaks were scanned from 10-300 K in 10 K steps for the characterization of the phase transition. To provide a clear distinction when discussing the details of the crystal structure: a , b , and c are used for the lattice constants in the orthorhombic unit cell whereas a_m , b_m , and c_m are used for the lattice constants in the monoclinic unit cell.

To further investigate structural properties, neutron diffraction measurements on polycrystalline samples of $\text{CeCu}_{6-x}\text{Ag}_x$ ($x = 0, 0.035, 0.1$) and $\text{CeCu}_{6-x}\text{Pd}_x$ ($x = 0.05, 0.1, 0.4$) were performed using the HB-2A powder diffractometer at HFIR using incident neutrons with wavelength of $\lambda = 1.54$ Å. In each case, ~ 5 g of polycrystalline sample was held in a cylindrical vanadium can with Helium as an exchange gas. The vanadium can was loaded in a top loading closed cycle refrigerator. Diffraction patterns above and below T_s were collected. A single crystal of $\text{CeCu}_{5.95}\text{Ag}_{0.05}$ was measured using the HB-3A four-circle diffractometer at HFIR with an incident wavelength of $\lambda = 1.003$ Å. The temperature dependence of the several structural peaks was measured to estimate T_s .

The magnetic susceptibilities of several polycrystalline samples ($x = 0.05, 0.3, 0.9$ and 1.2 of $\text{CeCu}_{6-x}\text{Ag}_x$, and $x = 0.05, 0.15, 0.25, 0.35$ and 0.4 of $\text{CeCu}_{6-x}\text{Pd}_x$) were measured using a Quantum Design magnetic property measurement system (MPMS) between 2 K - 300 K with an applied field of 1 kOe. RUS measurements were obtained for polycrystalline samples of $\text{CeCu}_{6-x}\text{Ag}_x$ ($x = 0.025, 0.05, 0.09$) using a custom-designed probe in a Quantum Design physical properties measurement system (PPMS). The temperature dependence of the resonances was measured within the frequency range 500-1000 kHz.

Rietveld analysis of the x-ray and neutron diffraction patterns was performed using the FullProf software package[40]. A representational analysis was performed using SARAh[41] to illuminate symmetry allowed magnetic structures.

III. RESULTS

A. Characterization

Energy-Dispersive x-ray Spectroscopy (EDS) analysis performed on several samples indicate that the sam-

ples are homogeneous and the elemental composition is in good agreement with their nominal values. Room-temperature laboratory x-ray diffraction was used for phase identification and as a check of sample purity. Synchrotron x-ray diffraction measurements on the sample compositions noted above were utilized as an additional check of the phase purity of the samples. The only evidence of an impurity phase in the samples studied here is the presence in the synchrotron x-ray diffraction patterns of a single unidentified peak smaller than 0.25% of the most intense structural peak of CeCu_6 . This peak was not observed in the neutron diffraction or the laboratory x-ray measurements.

DC magnetic susceptibility measurements of several samples are shown in Fig. 2. A linear dependence of the inverse magnetic susceptibility is observed over a large region of temperature indicating Curie-Weiss behavior.

Using the Curie-Weiss relation, $\chi = \chi_0 + \frac{N_A \mu_{eff}^2}{3k_B(T - \theta_{CW})}$, the effective values of the magnetic moment are estimated from the fits of susceptibility data between 200 K - 300 K. The magnetic moments for different compositions of $\text{CeCu}_{6-x}\text{T}_x$ ($T = \text{Ag, Pd}$) are close to the expected value ($\mu_{eff} = 2.54 \mu_B$) of the Ce^{3+} moment and are 2.42(1) μ_B , 2.43(1) μ_B , 2.67(1) μ_B and 2.50(1) μ_B for CeCu_6 , $\text{CeCu}_{5.65}\text{Pd}_{0.35}$, $\text{CeCu}_{5.1}\text{Ag}_{0.9}$ and $\text{CeCu}_{5.85}\text{Pd}_{0.15}$ respectively.

B. Neutron & x-ray Diffraction

The crystal structure of CeCu_6 is known to be orthorhombic with space group $Pnma$ at room-temperature[42, 43]. The orthorhombic unit cell consists of one general $8d$ site and five $4c$ sites. The Cerium atoms occupy one of the $4c$ positions whereas the Cu atoms are distributed among the general $8d$ and four $4c$ sites[42, 43]. This crystal structure is used as a model for the analysis of the diffraction patterns of $\text{CeCu}_{6-x}\text{Ag}_x$ and $\text{CeCu}_{6-x}\text{Pd}_x$. All the compositions of $\text{CeCu}_{6-x}\text{Ag}_x$ and $\text{CeCu}_{6-x}\text{Pd}_x$ that we have studied are isomorphous to the parent compound CeCu_6 at room temperature. The lattice parameter b slightly decreases with Ag/Pd substitution while the parameters a and c increase along with an overall expansion of the unit cell volume in both

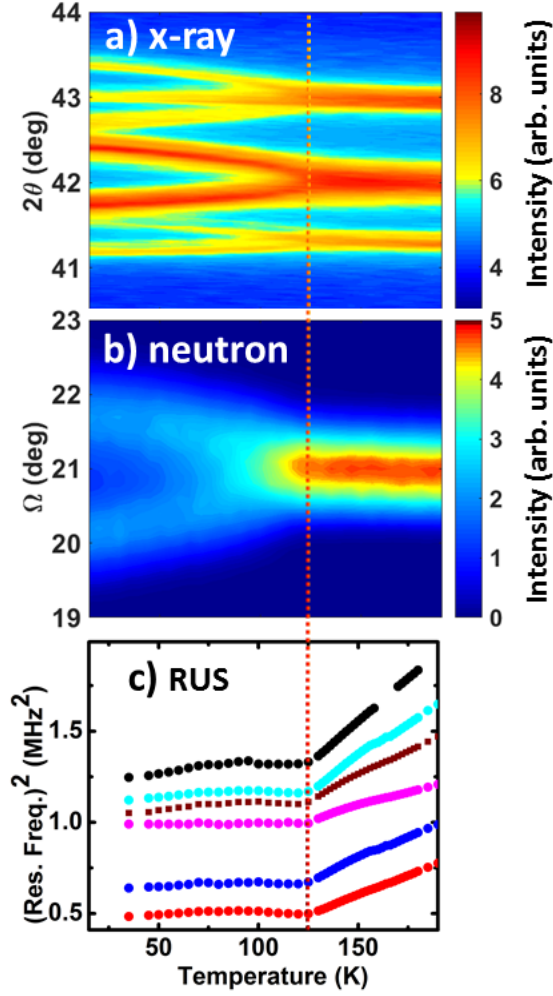


FIG. 3. (Color online) The structural transition of $\text{CeCu}_{5.95}\text{Ag}_{0.05}$ characterized using a) powder x-ray diffraction: The (122), (220) and (221) structural peaks in the orthorhombic phase split in the monoclinic phase as described in the text. Note that peaks indexed as (h 0 l) or (0 k l) in the orthorhombic phase are unaltered, aside from a change of indexing, by the monoclinic distortion. b) Single crystal neutron diffraction: The structural peak (2 2 0) of orthorhombic phase splits into two structural peaks (2 0 2) and (-2 0 2) of monoclinic phase at T_s . c) RUS: the square of the resonant frequencies change slope at T_s . A vertical line in the plot shows T_s . All measurements indicate that the structural phase transition takes place in $\text{CeCu}_{5.95}\text{Ag}_{0.05}$ at $T_s \approx 125(5)$ K.

systems. The synchrotron x-ray diffraction patterns and the fit obtained from the Rietveld refinements of CeCu_6 , $\text{CeCu}_{5.7}\text{Ag}_{0.3}$ and $\text{CeCu}_{5.7}\text{Pd}_{0.3}$ are shown in Fig. 1, and the results of the fit are summarized in Tables I and II.

The coherent neutron scattering lengths of the dopants, Ag ($= 5.92$ fm) and Pd ($= 5.91$ fm), are close to that of copper ($= 7.72$ fm). This low contrast coupled with the small amount of dopants present renders the determination of the site occupancy with neutron scattering inconclusive. Therefore, high-resolution synchrotron x-

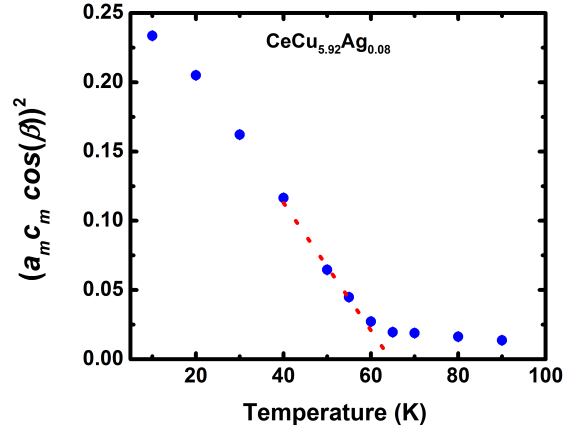


FIG. 4. (Color online) Monoclinic order parameter $((a_m c_m \cos(\beta))^2)$ of $\text{CeCu}_{5.92}\text{Ag}_{0.08}$ obtained from neutron diffraction measurements. An extrapolation of the order parameter gives $T_s = 62(3)$ K. A continuous change in the monoclinic order parameter is observed near T_s .

ray diffraction was used for this purpose. Rietveld refinement of the synchrotron x-ray diffraction measurement indicates that the Ag-atoms in $\text{CeCu}_{6-x}\text{Ag}_x$ are not distributed between different copper sites, but prefer the Cu2 site of the $Pnma$ structure. This is similar to $\text{CeCu}_{6-x}\text{Au}_x$ system, where Au-atoms occupy the Cu2 site until the site is fully occupied[42, 44]. A different situation occurs in $\text{CeCu}_{6-x}\text{Pd}_x$, where the Pd-atoms occupy multiple Cu sites. The analysis of the synchrotron x-ray diffraction pattern shows that the majority of the Pd atoms occupy the Cu2 site and the remaining Pd atoms are distributed on Cu1 and Cu4 sites. The precise value of the Pd-occupancies on all other sites except Cu2 are difficult to determine as the occupancies on these sites are very small and are near the limit of what is possible for this analysis. The Pd-occupancies that give the best fit of the diffraction pattern are shown in Fig. 1(c) and are tabulated in the Table I(b).

C. Structural Phase Transitions

Fig. 3 illustrates the different methods used for the characterization of the structural phase transitions: x-ray diffraction, neutron diffraction, and RUS. To check the consistency in these measurements and the quality of the samples, $\text{CeCu}_{5.95}\text{Ag}_{0.05}$ was grown in both polycrystalline and single crystal forms and measured by all three techniques. A small part of the Czochralski-grown single crystal was measured with neutron diffraction, and different batches of the polycrystalline samples were measured by x-ray diffraction and RUS. The transition temperature (T_s) of $\text{CeCu}_{5.95}\text{Ag}_{0.05}$ was estimated to be at $T_s = 125(1)$ K using neutron diffraction. The RUS and x-ray diffraction measurements of the polycrystalline $\text{CeCu}_{5.95}\text{Ag}_{0.05}$ yield $T_s = 122(1)$ K and $T_s = 125(5)$ K respectively. This

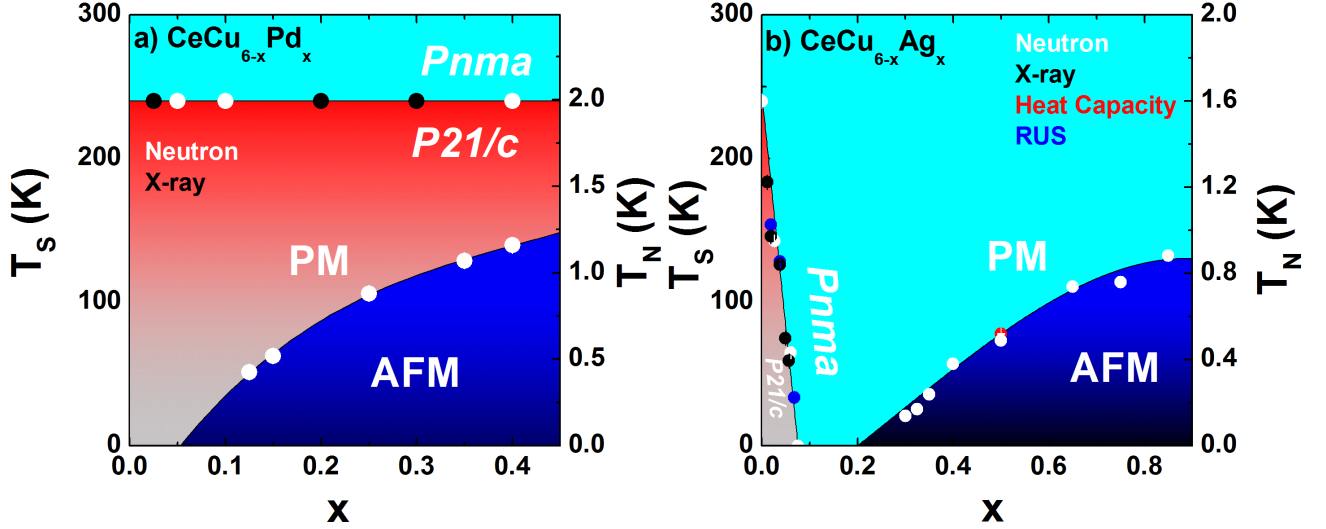


FIG. 5. (Color online) The phase diagrams of a) $\text{CeCu}_{6-x}\text{Pd}_x$ and b) $\text{CeCu}_{6-x}\text{Ag}_x$. The concentration for the occurrence of the magnetic QCP is taken to be the same as in [35, 37] and is $x_{\text{QCP}} \approx 0.2$ for $\text{CeCu}_{6-x}\text{Ag}_x$ and $x_{\text{QCP}} \approx 0.05$ for $\text{CeCu}_{6-x}\text{Pd}_x$. In $\text{CeCu}_{6-x}\text{Ag}_x$, the termination of the structural phase transition occurs at $x_S \approx 0.1$. No suppression of the structural phase transition was observed in $\text{CeCu}_{6-x}\text{Pd}_x$ for $x \leq 0.4$.

attests to the consistency of the measurement techniques.

The monoclinic order parameter $((a_m c_m \cos(\beta))^2)$ changes smoothly with temperature near T_s (Fig. 4). The structural peaks that are indexed as (h k l) in space group *Pnma* split into two structural peaks which are indexed as $(-k l h)$ and $(k l h)$ in the monoclinic space group *P2₁/c*. The splitting of the structural peaks at T_s can be explicitly observed in the temperature dependence of the diffraction pattern as shown in Fig. 3(a), where the peaks in *Pnma* phase split into *P2₁/c*-peaks as $(1\ 2\ 2) \rightarrow (-2\ 2\ 1) + (2\ 2\ 1)$, $(2\ 2\ 0) \rightarrow (-2\ 0\ 2) + (2\ 0\ 2)$ and $(2\ 2\ 1) \rightarrow (-2\ 1\ 2) + (2\ 1\ 2)$. The splitting of these peaks is also confirmed by single crystal neutron diffraction measurements, a part of which is shown in Fig. 3(b).

RUS measurements are one of the most sensitive ways of characterizing structural phase transitions. The resonances occur as the natural frequency of the sample, which is closely related to its elastic properties, matches the incident ultrasonic wave. At T_s , the change in the elastic properties of the sample indicates the occurrence of the structural phase transition. Here, the temperature dependence of the square of the resonant frequency is used to show the structural phase transition. As shown in Fig. 3(c), the square of the resonant frequency versus temperature has a constant slope above T_s . The slope of the curve changes continuously at T_s , and the shift in the resonances below T_s are much weaker as compared to those at above T_s .

The work presented here indicates the structural phase transition from orthorhombic to monoclinic phase in CeCu_6 occurs at $T_s \approx 240$ K, which is somewhat larger compared to the previous studies[28, 29, 45]. The val-

ues of T_s in $\text{CeCu}_{6-x}\text{Ag}_x$ drop linearly with Ag concentration until the structural phase transition disappears above the critical composition, $x_S \geq 0.1$ (Fig. 5(b)). For $0.1 \leq x \leq 0.85$, no structural phase transition was observed above 4 K. The suppression of the structural phase transition due to doping is analogous to $\text{CeCu}_{6-x}\text{Au}_x$, where T_s drops in similar fashion and the termination of the structural phase transition occurs at a similar Au-composition, $x_S \approx 0.14$ [26, 27]. However, in $\text{CeCu}_{6-x}\text{Pd}_x$, no change in T_s is observed with Pd-substitution within the range of our investigation, ($0 \leq x \leq 0.4$). The changes in the transition temperatures with doping in $\text{CeCu}_{6-x}\text{Ag}_x$ and $\text{CeCu}_{6-x}\text{Pd}_x$ are summarized in the phase diagrams presented in Fig. 5.

D. First Principles Calculations

In an attempt to understand the observed doping dependence of the structural phase transitions –in particular, the appearance of the monoclinic state in the undoped CeCu_6 , the disappearance of this structural transition with Ag doping, and the unaltered transition temperature with Pd doping – all electron first principles calculations using the linearized augmented planewave code WIEN2K [46] have been performed. The generalized gradient approximation (GGA) of Perdew, Burke and Ernzerhof [47] was used, with sphere radii for the undoped compound of 2.21 Bohr for Cu and 2.50 for Ce. For the undoped compound, we used the lattice parameters and angles of the orthorhombic and low-temperature monoclinic phases reported by Asano *et al.* [48], and relaxed

TABLE III. The relative energies of several configurations for Ag and Pd doping. “SP” refers to a spin-polarized calculation.

Configuration	ΔE (meV/u.c.)
Ag doping – orthorhombic	0
Ag doping – orthorhombic SP	-4
Ag doping – monoclinic	+95
Ag doping – monoclinic SP	+92
Pd doping (Cu2) - orthorhombic	0
Pd doping (Cu2) - orthorhombic SP	+1
Pd doping (Cu2)- monoclinic	+74
Pd doping (Cu2) - monoclinic SP	+ 73
Pd doping (Cu1) - orthorhombic	0
Pd doping (Cu1) - monoclinic	+ 82

the internal coordinates until forces on the atoms were less than 2 mRyd/Bohr. An RK_{max} – the product of the smallest sphere radius and largest planewave vector – of 9.0 was used. All calculations, the relaxation excepted, were performed with spin-orbit coupling included and for the doped calculations we also allowed for spin polarization. Sufficient numbers of k points – as many as 10,000 in the full Brillouin zone – were used, though in later calculations we found that less than 1000 such points were necessary for convergence of energy differences.

For the calculations of the effect of Ag and Pd doping on the structural phase transition, several assumptions concerning the structure were necessary. As detailed in Table II, in the high temperature orthorhombic phase, for a doping level $x=0.1$, the structures for $CeCu_{5.9}Ag_{0.1}$ and $CeCu_{5.9}Pd_{0.1}$ are very similar, differing in volume by less than 0.2 percent. Since even at this doping level the experimentally observed properties are very different (orthorhombic groundstate for Ag doping, monoclinic groundstate for Pd doping), it was decided to isolate the effects of charge doping from the small structural differences by using the same lattice parameters and internal coordinates for Ag doping and Pd doping. In each case one of the 24 Cu atoms in the unit cell was replaced by Cu or Pd. Since there is a substantial site preference for Ag doping in this case we used the Cu2 site for the substitution. For Pd doping, two separate sets of calculations were done, one with the Pd atom at the Cu1 site, and the other with the Pd atom at the Cu2 site. The structural parameters used for the orthorhombic phase were those for $x_{Ag} = 0.1$ at room temperature, while for the monoclinic phase the parameters for $x_{Pd} = 0.1$ at 4 K were used. There is, of course, no experimental monoclinic structure available for Ag doping, but for an energy comparison use of the Pd-based structure was considered sufficient.

We begin the discussion of our results with those found for $CeCu_6$. The optimized monoclinic structure has an energy 33 meV per unit cell (note there are 4 formula units per unit cell) lower than the optimized orthorhombic structure, consistent with experimental observation. Despite this energy difference, the changes in electronic structure upon passing through the transition are scant.

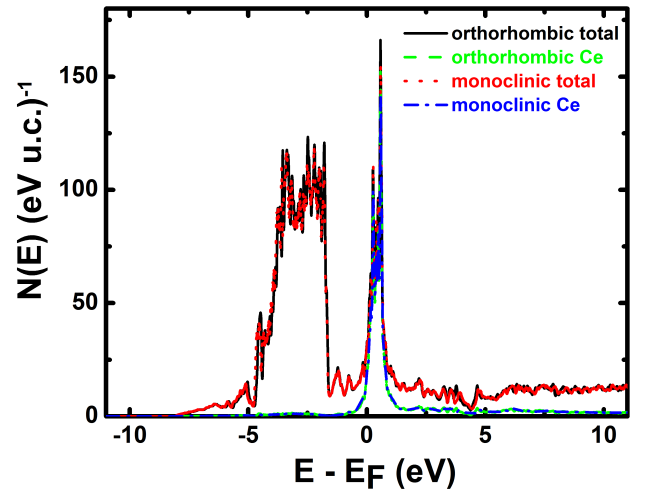


FIG. 6. (Color online) The calculated density-of-states of $CeCu_6$ in the orthorhombic and monoclinic structures.

Figure 6 presents a plot of the calculated density-of-states (DOS) for both cases. In both cases there is a peak in the DOS slightly above the Fermi level, attributable to the Ce states, along with a large valence band contribution between 2 and 5 eV beneath E_F . The Fermi level DOS, at 31.53/eV - unit cell for the orthorhombic cell and 30.82/eV - unit cell for the monoclinic, changes by only 2 percent across the transition.

Regarding the doped compounds, in Table III we present our results, for both Ag and Pd doping, for the relative energies, per unit cell of the monoclinic and orthorhombic states, both with and without spin polarization. For simplicity, the non-spin polarized orthorhombic state was chosen as the zero of energy. Note that in the spin-polarized calculations, to make the calculation tractable, a ferromagnetic configuration of the Ce atoms has been assumed rather than the incommensurate antiferromagnetism that is actually observed. Given the Ce-Ce distances of 4.85 Å and the very low (~ 1 K or less) experimental magnetic ordering temperatures, the energies of the assorted Ce spin configurations whose competition sets the Neel temperature are likely within 1 K \sim 0.1 meV per Ce, which is within our calculational resolution.

Table III shows that the calculations correctly predict the suppression of the monoclinic state with Ag doping - the monoclinic state lies 95 meV higher in energy than the orthorhombic state, and including spin polarization does not appreciably change this result. The spin-polarized orthorhombic state, with a calculated Ce moment of $0.34 \mu_B$, appears to be the groundstate, lying some 4 meV beneath the non spin-polarized orthorhombic state, and well above both monoclinic states.

The calculations, however, also predict, in contrast to experiment, the suppression of the monoclinic state for Pd doping. For Pd doping on Cu2 site this state is 74 meV above the orthorhombic state, and including spin polarization does not remedy this. A similar result is ob-

tained for doping on the Cu1 site (spin polarization was not checked in this case), with an 82 meV energy difference. These energy differences are, at least, smaller than that found for Ag doping, but they are still significant and the discrepancy with experiment does not likely arise due to convergence issues.

While the reason for the divergence of theory and experiment for the structural effects of Pd doping is not clear, it is plausible that it arises due to the heavy fermion state, which along with quantum critical physics tends to confound mean-field based density functional theory. For example, for the base CeCu₆ our calculated T-linear specific heat coefficient γ is 18.2 mJ/mol-K², much smaller than the observed value of between 840 and 1600 mJ/mol-K² [49]. It is also possible that our neglect of correlations (i.e., no use of GGA+U) on the Ce atom has some effect. It should also be pointed out that it is impractical to rigorously prove the *lack* of a symmetry-breaking structural distortion, given the existence of a continuous variable (in this case the monoclinic angle) which would need to be carefully scanned for energy minima. However, the fact that the calculations do correctly predict the groundstate of CeCu₆, along with that for Ag doping, gives hope for the ability of first principles calculations to ultimately describe this system.

E. Magnetic Phase Transitions

Using the information obtained from the study of the polycrystalline samples together with the CeCu_{6-x}Au_x literature, magnetic reflections in the (h 0 l) scattering plane were measured in CeCu_{6-x}Ag_x and CeCu_{6-x}Pd_x (for example see Fig. 7). For simplicity and ease of comparison with the work presented here on CeCu_{6-x}Ag_x as well as the extensive work on CeCu_{6-x}Au_x, we neglect the small monoclinic distortion (less than 2°) in CeCu_{6-x}Pd_x and use orthorhombic notation to discuss the magnetic properties.

The magnetic Bragg reflections occurs at the points in the reciprocal space that satisfies the condition $\mathbf{Q} = \boldsymbol{\tau} \pm \mathbf{k}_i$ ($i = 1, 2$), where $\boldsymbol{\tau}$ represents a nuclear reciprocal vector and \mathbf{k}_i are the incommensurate propagation vector, $\mathbf{k}_1 = (0.62 \ 0 \ 0.3)$, or the symmetry equivalent $\mathbf{k}_2 = (0.62 \ 0 \ -0.3)$. The change in magnetic propagation vector with Ag/Pd doping is presented in Table IV. The magnetic propagation vector for CeCu_{6-x}Ag_x is only weakly dependent on composition. The change in the magnitude of the propagation vector with doping appears to be more pronounced in CeCu_{6-x}Pd_x. For higher Pd-compositions ($x \geq 0.25$), measurements were performed on polycrystalline samples, for which a continuous change in the absolute value of the magnetic wave vector is observed.

The intensities of a structural or a magnetic peak collected with a triple-axis instrument is the convolution of the Bragg intensity with the instrumental resolution function. The software package ResLib[50] was utilized to estimate the instrumental resolution and thereby enable

TABLE IV. Compositional dependence of the magnetic wave vector in CeCu_{6-x}Ag_x and CeCu_{6-x}Pd_x.

CeCu _{6-x} Ag _x		
x	\mathbf{Q} (h k l) [r.l.u.]	$ \mathbf{Q} $ (Å ⁻¹)
0.85	—	0.499(2)
0.75	(0.615(1) 0 0.302(1))	0.504(1)
0.65	—	0.501(2)
0.50	(0.633(1) 0 0.296(1))	0.522(1)
0.40	(0.641(1) 0 0.301(1))	0.521(1)
0.35	(0.645(2) 0 0.300(1))	0.518(1)
0.30	(0.646(1) 0 0.297(1))	0.529(1)
CeCu _{6-x} Pd _x		
x	\mathbf{Q} (h k l) [r.l.u.]	$ \mathbf{Q} $ (Å ⁻¹)
0.40	—	0.449(3)
0.35	—	0.466(6)
0.25	—	0.480(4)
0.15	(0.624(1) 0 0.250(1))	0.509(1)
0.125	(0.624(1) 0 0.253(1))	0.510(1)

TABLE V. Basis vectors from representational analysis of space group $Pnma$ with $\mathbf{k} = (0.62, 0, 0.3)$. The Ce-site is separated into four orbits given by 1: (0.2586, 0.25, 0.5636), 2: (0.2414, 0.75, 0.06360), 3: (0.7414, 0.75, 0.4364), 4: (0.7586, 0.25, 0.9364). The decomposition of the magnetic representation for each of the four orbits is $\Gamma_{Mag} = 1\Gamma_1^1 + 2\Gamma_2^1$. Symbols $m_{\parallel a}$, $m_{\parallel b}$, $m_{\parallel c}$ denote the projection of the magnetic moment along the a , b and c -axis respectively.

IR	BV	BV components					
		$m_{\parallel a}$	$m_{\parallel b}$	$m_{\parallel c}$	$im_{\parallel a}$	$im_{\parallel b}$	$im_{\parallel c}$
Γ_1	$\boldsymbol{\psi}_1$	0	1	0	0	0	0
Γ_2	$\boldsymbol{\psi}_2$	1	0	0	0	0	0
	$\boldsymbol{\psi}_3$	0	0	1	0	0	0

the extraction of resolution corrected intensities using the Cooper-Nathans approximation[51]. For CeCu_{5.25}Ag_{0.75} the calculated instrumental resolution is indicated by the horizontal lines in Fig. 7(b) and 7(c). The instrumental resolution is not isotropic in the scattering plane and results in an elliptically shaped Bragg peak (e.g. inset of Fig. 7(a)). The magnetic Bragg peaks observed for all compositions are found to be resolution limited, consistent with the presence of the long range magnetic order.

After the correction for instrumental resolution, magnetic peaks were normalized to the intensity of the nearby structural peak (0 0 2). The resulting order parameter data is used to characterize the magnetic phase transition. The Neel temperatures (T_N) are estimated by fitting the power law equation, $y = y_0 + A(T - T_N)^{2\beta}$. β was constrained to the mean field value of 0.5. Mean field behavior has previously been observed near the QCP in other heavy fermion systems[23, 52–54]. This is likely due to the change in the effective dimension of the system as the quantum dynamics influences the static critical properties—one of the most prominent distinctions from a counterpart classical phase transition. The fits of the order parameters for several compositions of CeCu_{6-x}Ag_x and CeCu_{6-x}Pd_x are shown in Fig. 8. The Neel temper-

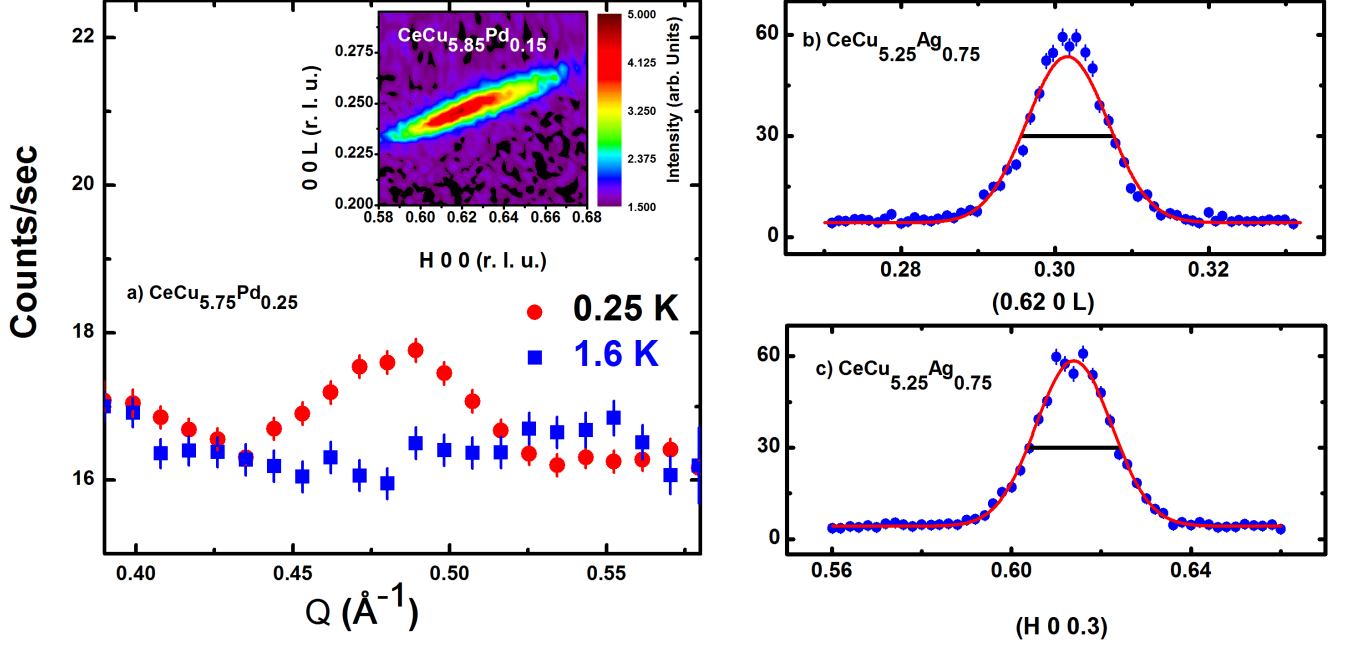


FIG. 7. (Color online) a) The magnetic reflection at $Q = 0.480(3)$ from a polycrystalline sample with a composition of $\text{CeCu}_{5.75}\text{Pd}_{0.25}$. The inset shows the magnetic reflection from a single crystal of $\text{CeCu}_{5.85}\text{Pd}_{0.15}$ near the wave vector $\mathbf{Q} = (0.6243(1) \ 0 \ 0.2503(1))$. b) and c) Single crystal diffraction measurement of the the $(0.62 \ 0 \ 0.3)$ magnetic reflection of $\text{CeCu}_{5.25}\text{Ag}_{0.75}$ along $(0.62 \ 0 \ L)$ and $(H \ 0 \ 0.3)$ at 0.05 K. The red line is a Gaussian fit to the data constrained by the instrumental resolution. The horizontal black lines are the calculated instrumental resolution.

atures (T_N) estimated from the elastic neutron scattering measurements are in good agreement with the magnetic susceptibility and heat capacity measurements of previous studies[32, 35]. The estimated values of T_N in $\text{CeCu}_{6-x}\text{Ag}_x$ and $\text{CeCu}_{6-x}\text{Pd}_x$ are incorporated in the phase diagrams presented in Fig. 5.

For the wave vector $\mathbf{k}_1 = (0.62 \ 0 \ 0.3)$ and space group $Pnma$, representational analysis indicates the four equivalent Ce positions in the unit cell split into separate orbits as given by 1: $(0.2586, 0.25, 0.5636)$, 2: $(0.2414, 0.75, 0.06360)$, 3: $(0.7414, 0.75, 0.4364)$, 4: $(0.7586, 0.25, 0.9364)$. Two irreducible representations (IR) are found for all four orbits with their basis vectors as listed in Table V. To understand the magnetic structure in greater detail, we focus on $\text{CeCu}_{5.5}\text{Ag}_{0.5}$ ($T_N = 0.51(1)$ K). Following the representational analysis, the first IR, Γ_1 , restricts the arrangement of Ce-moments to be parallel to the b -axis. Given that the propagation vector indicates a modulation in the ac -plane, only a transverse modulation of the magnetic moment is possible under this representation. Structures of this type can be discarded as the observed intensities do not match with the calculated intensities. The second IR, Γ_2 , restricts moments to the ac -plane but limits the possible magnetic structures to those with a modulation of the magnetic moment amplitude or a cycloidal modulation of the moment direction. However, the cycloidal model does not account well for the intensities of the observed magnetic reflections. The remain-

ing possibility is a sinusoidal modulation of the moment amplitude in the crystallographic ac -plane. To simplify the problem, the directions of the Ce-moments were constrained to be same for all four Ce-orbits but the phases were allowed to vary. The best fit under this assumption was obtained when the moments point along the c -axis with a magnitude of $0.61(1) \ \mu_B$. This yields the magnetic structure shown in the Figure 9(a), which is also consistent with the previous studies on $\text{CeCu}_{6-x}\text{Au}_x$ that report a similar structure based on neutron diffraction measurements[20, 23, 55–57]. The comparison between the observed and the calculated intensities is shown in the Figure 9(b).

The ordered moment obtained from a neutron diffraction measurement is proportional to the square root of the intensity of the magnetic Bragg peak, which is generally scaled to the nuclear reflections to provide an absolute value. Assuming that the magnetic structure doesn't change with Ag/Pd-doping, the moments of other compositions were determined from a comparison of the normalized magnetic intensity with respect to that of $\text{CeCu}_{5.5}\text{Ag}_{0.5}$. In both systems, the magnitude of the moment increases with Ag/Pd-doping as shown in the Figure 9(c). We note though, that the full saturated moment was not obtained for several compositions near the QCP and these compositions are indicated by triangles in Fig. 9(c).

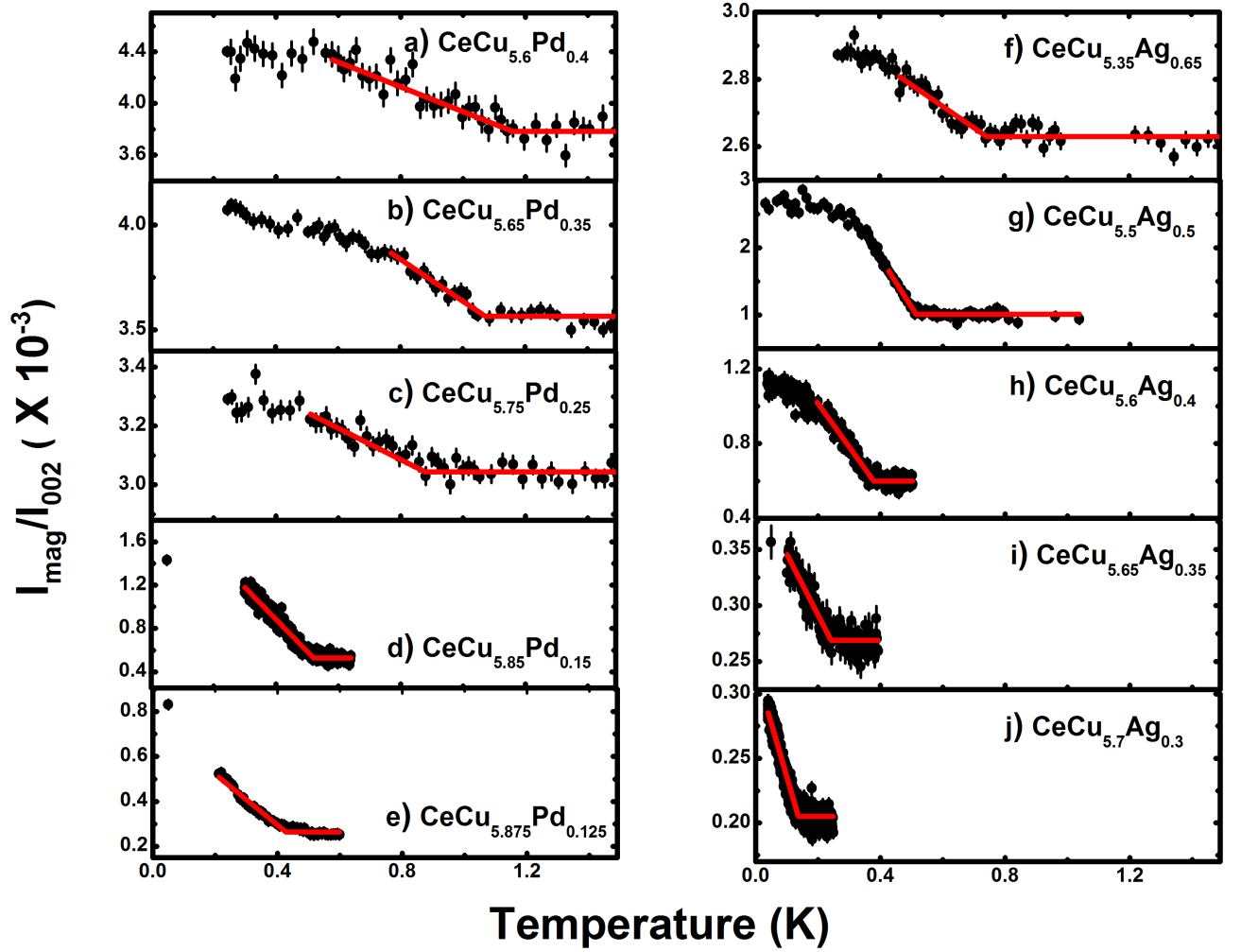


FIG. 8. (Color online) Temperature dependence of the intensity of the magnetic peak ((0.62 0 0.25) for $\text{CeCu}_{6-x}\text{Pd}_x$ and (0.64 0 0.3) for $\text{CeCu}_{6-x}\text{Ag}_x$) normalized to the structural (0 0 2) peak in (a-e) $\text{CeCu}_{6-x}\text{Pd}_x$ and (f-j) $\text{CeCu}_{6-x}\text{Ag}_x$. The red line is a fit to the data with a power law equation of the form $y = y_0 + A(T - T_N)^{2\beta}$. β was fixed to the mean field value of 0.5 and T_N was allowed to vary in order to estimate the transition temperature. The estimated values of T_N are a) 1.16(3) K, b) 1.07(2) K, c) 0.88(3) K, d) 0.52(1) K, e) 0.43(1) K, f) 0.74(2) K, g) 0.51(1) K, h) 0.38(1), i) 0.24(1) K, j), and 0.14(1) K.

IV. DISCUSSION

It is interesting to view the results presented here on $\text{CeCu}_{6-x}\text{Pd}_x$ and $\text{CeCu}_{6-x}\text{Ag}_x$ in the context of the structural and magnetic properties of the intensively studied $\text{CeCu}_{6-x}\text{Au}_x$ system. Inelastic neutron scattering measurements at the QCP of $\text{CeCu}_{6-x}\text{Au}_x$ show the presence of critical spin fluctuations peaked at $\mathbf{Q} = (0.8 \ 0 \ 0)$, but present in an extended region of the Brillouin zone in the shape of a butterfly[19, 20]. Interestingly, the points at the wings of the butterfly correspond to the magnetic ordering wave vectors observed for different Au-compositions of $\text{CeCu}_{6-x}\text{Au}_x$ in the magnetically ordered regime[23–25, 54, 58]. Among all the compositions of $\text{CeCu}_{6-x}\text{Au}_x$ that are reported, the composition $x = 0.2$, studied by neutron diffraction closest to the QCP,

is the only one which exhibits short ranged magnetic ordering near the wave vector $\mathbf{Q} = (0.8 \ 0 \ 0)$ in addition to a long range magnetic ordering that occurs at $\mathbf{Q} = (0.625 \ 0 \ 0.275)$ [54–56, 59]. With a slight increase in Au-composition, for $x = 0.3$, the short range order disappears and only the long range magnetic ordering is observed at the wave vector $\mathbf{Q} = (0.64 \ 0 \ 0.275)$ [54, 56, 59]. Upon further alloying with Au, at $x = 0.5$, the magnetic wave vector exhibits a crossover to $\mathbf{Q} = (0.59 \ 0 \ 0)$, which stays roughly the same for higher Au-composition [54, 56, 59, 60]. However, in $\text{CeCu}_{6-x}\text{Ag}_x$ and $\text{CeCu}_{6-x}\text{Pd}_x$, our studies find no evidence for short range magnetic order near $\mathbf{Q} = (0.8 \ 0 \ 0)$. Furthermore, in $\text{CeCu}_{6-x}\text{Ag}_x$, the magnetic propagation vector is essentially unchanged for the range of the compositions investigated here suggesting there is no crossover to a propagation vector near $\mathbf{Q} = (0.59 \ 0 \ 0)$ at large x . The possibility of such a crossover in the magnetic

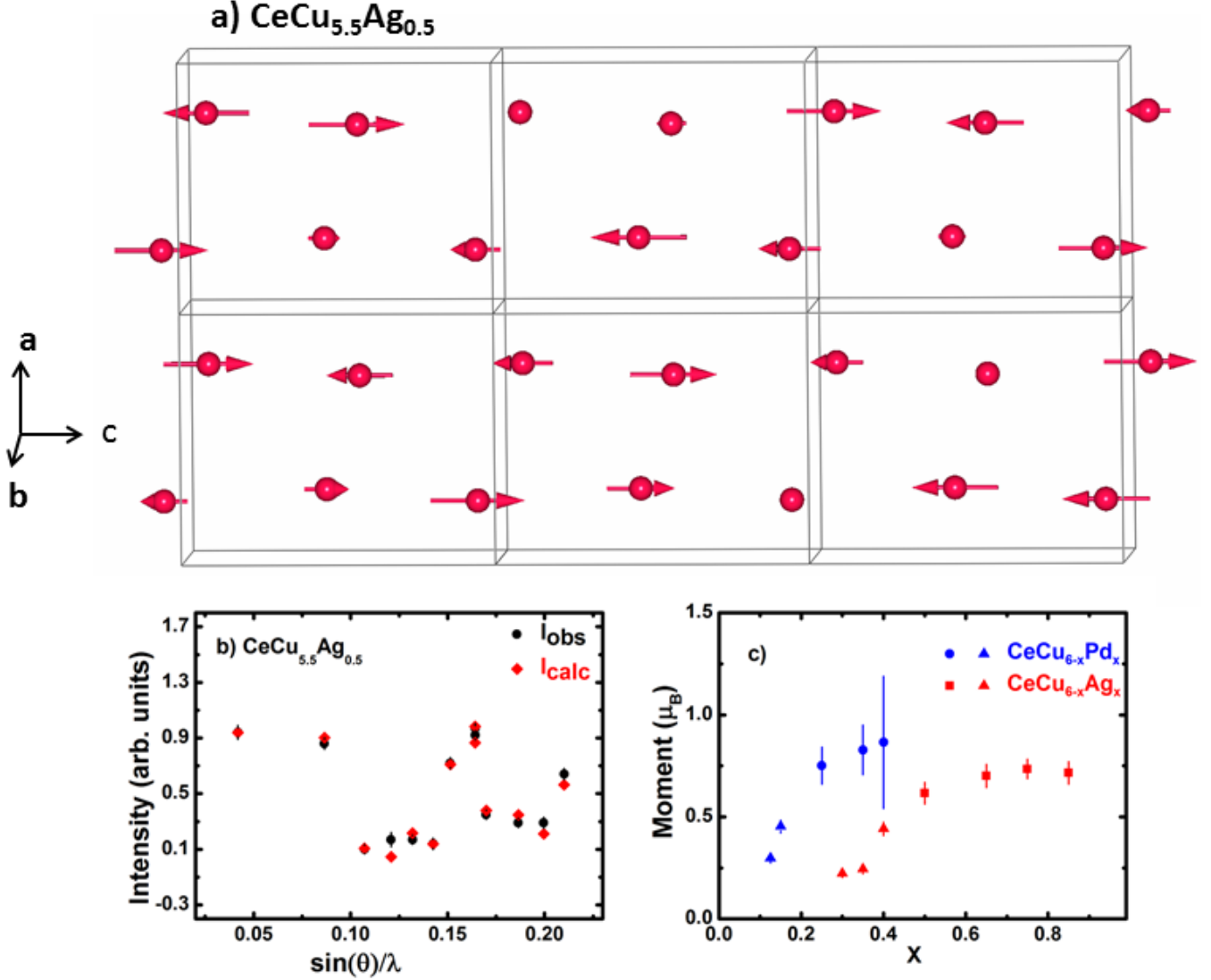


FIG. 9. (Color online) a) The magnetic structure of $\text{CeCu}_{5.5}\text{Ag}_{0.5}$. Each box represents a structural unit cell that contains four Ce-atoms as indicated by the red spheres. The length and direction of the arrows show the magnitude and direction of the moment, respectively. All Ce-moments point along the c -axis of the orthorhombic crystal structure. The amplitude of the moment is modulated along the wave vector $(0.62 \ 0 \ 0.3)$ b) The fit of the magnetic structure showing observed and calculated intensities of different magnetic reflections of $\text{CeCu}_{5.5}\text{Ag}_{0.5}$. c) Compositional dependence of the ordered moments in $\text{CeCu}_{6-x}\text{T}_x$ ($T = \text{Ag}, \text{Pd}$). The magnetic structure was determined for $\text{CeCu}_{5.5}\text{Ag}_{0.5}$ and was assumed to be the same for the remainder of the compositions. A point shown as a triangle indicates a composition for which the magnetic moment was not completely saturated and thus the full moment value will be somewhat larger.

propagation vector at large x in $\text{CeCu}_{6-x}\text{Pd}_x$ cannot be entirely excluded as the measurements were performed with polycrystalline samples for higher Pd-compositions.

The possibility that the structural degrees of freedom could give rise to a quantum multicritical point in $\text{CeCu}_{6-x}\text{Au}_x$ [27] is interesting and worthy of further consideration. Among the three systems $\text{CeCu}_{6-x}\text{Ag}_x$, $\text{CeCu}_{6-x}\text{Pd}_x$, and $\text{CeCu}_{6-x}\text{Au}_x$: $\text{CeCu}_{6-x}\text{Ag}_x$ is the only system where the magnetic QCP occurs in the orthorhom-

bic phase, and is well-separated from the termination of the structural phase transition. On the other hand, in $\text{CeCu}_{6-x}\text{Pd}_x$, the magnetic QCP occurs in the monoclinic phase but is clearly distinct from any structural phase transition. The disparity in the structural properties among these systems offers an opportunity where the unconventional QCP observed in $\text{CeCu}_{6-x}\text{Au}_x$ can be investigated without the complications introduced by a nearby structural phase transition. Despite the distinct behav-

ior of the structural and magnetic phase transitions in $\text{CeCu}_{6-x}\text{Au}_x$, $\text{CeCu}_{6-x}\text{Ag}_x$, $\text{CeCu}_{6-x}\text{Pd}_x$ the heat capacity in all three systems appears to exhibit a similar logarithmic divergence at low temperature [35, 39, 61]. This suggests the thermal average of the underlying critical fluctuations is essentially unaltered by the different structural properties. Nevertheless, further work in this area is probably warranted and $\text{CeCu}_{6-x}\text{Ag}_x$ and $\text{CeCu}_{6-x}\text{Pd}_x$ would be ideal candidates for such studies.

The orthorhombic-monoclinic structural phase transition in CeCu_6 is second order in nature [30]. We have uncovered no evidence either in the temperature dependence of the monoclinic order parameter $(a_m c_m \cos \beta)^2$ or in the square of the resonance frequencies determined from the RUS measurements that the transition becomes first order with doping (See Fig. 3(c) and 4). Thus there appears to be the possibility that a complete suppression of the orthorhombic-monoclinic transition results in a structural QCP. The notion of the structural QCP is still emerging and has attracted recent attention. For example, the $(\text{Sr}, \text{Ca})_3\text{Ir}_4\text{Sn}_{13}$ series appears to exhibit a structural quantum critical point [62, 63]. Since any structural QCP in $\text{CeCu}_{6-x}\text{Au}_x$ or $\text{CeCu}_{6-x}\text{Ag}_x$ would be complicated by the presence of a magnetic QCP, investigating other CeCu_6 -derived systems or their non-magnetic analogs, such as $\text{LaCu}_{6-x}\text{Au}_x$, may be fertile grounds in which to further probe the concept of a structural QCP.

V. CONCLUSIONS

In conclusion, we report a comprehensive study of the structural and the magnetic properties of $\text{CeCu}_{6-x}\text{Ag}_x$ and $\text{CeCu}_{6-x}\text{Pd}_x$. Long range incommensurate magnetic ordering evolves with doping in both systems. The magnetic structure is composed of a sinusoidal modulation

of the Ce-moments aligned which are aligned along the crystallographic c -axis of the orthorhombic ($Pnma$) unit cell. The long range magnetic structure as well as the size of the ordered moments determined in $\text{CeCu}_{6-x}\text{Ag}_x$ and $\text{CeCu}_{6-x}\text{Pd}_x$ are similar to the well known heavy fermion system $\text{CeCu}_{6-x}\text{Au}_x$. Yet, these systems exhibit several unique structural and magnetic properties. The magnetic QCP in $\text{CeCu}_{6-x}\text{Ag}_x$ occurs in the orthorhombic phase and is well separated from the termination of the structural phase transition. No substantial change in the magnetic wave vector is observed with Ag-composition in $\text{CeCu}_{6-x}\text{Ag}_x$. In $\text{CeCu}_{6-x}\text{Pd}_x$, the magnetic QCP occurs well within the monoclinic phase. Further investigations of $\text{CeCu}_{6-x}\text{Ag}_x$ and $\text{CeCu}_{6-x}\text{Pd}_x$ are essential to understand the nature of QCP in these systems.

ACKNOWLEDGMENTS

We acknowledge JM Lawrence for useful discussions, M Suchomel for the technical assistance in synchrotron x-ray diffraction measurements, RE Baumbach and NJ Ghimire for their assistance in the sample preparation. The research at the High Flux Isotope Reactor (ORNL) is supported by the Scientific User Facilities Division, Office of Basic Energy Sciences, U.S. Department of Energy (DOE). Use of the Advanced Photon Source at Argonne National Laboratory was supported by the U. S. Department of Energy, Office of Science, Office of Basic Energy Sciences, under Contract No. DE-AC02-06CH11357. The laboratory XRD work was conducted at the Center for Nanophase Materials Sciences, which is a DOE Office of Science User Facility. HJ, HNL, AFM and DGM acknowledge the support from the U. S. Department of Energy, Office of Science, Basic Energy Sciences, Materials Sciences and Engineering Division.

-
- [1] J. A. Hertz, Phys. Rev. B **14**, 1165 (1976).
 - [2] A. J. Millis, Phys. Rev. B **48**, 7183 (1993).
 - [3] T. Moriya, *Spin fluctuations in itinerant electron magnetism*, Vol. 56 (Springer-Verlag Berlin, 1985).
 - [4] W. Knafo, S. Raymond, P. Lejay, and J. Flouquet, Nature Physics **5**, 753 (2009).
 - [5] H. v. Löhneysen, A. Rosch, M. Vojta, and P. Wölfle, Rev. Mod. Phys. **79**, 1015 (2007).
 - [6] H. Kadowaki, M. Sato, and S. Kawarazaki, Phys. Rev. Lett. **92**, 097204 (2004).
 - [7] R. Küchler, N. Oeschler, P. Gegenwart, T. Cichorek, K. Neumaier, O. Tegus, C. Geibel, J. A. Mydosh, F. Steglich, L. Zhu, and Q. Si, Phys. Rev. Lett. **91**, 066405 (2003).
 - [8] P. Gegenwart, C. Langhammer, C. Geibel, R. Helfrich, M. Lang, G. Sporn, F. Steglich, R. Horn, L. Donnevert, A. Link, and W. Assmus, Phys. Rev. Lett. **81**, 1501 (1998).
 - [9] C. H. Wang, L. Poudel, A. E. Taylor, J. M. Lawrence, A. D. Christianson, S. Chang, J. A. Rodriguez-Rivera, J. W. Lynn, A. A. Podlesnyak, G. Ehlers, R. E. Baumbach, E. D. Bauer, K. Gofryk, F. Ronning, K. J. McClellan, and J. D. Thompson, J. Phys. Condens. Matter **27**, 015602 (2015).
 - [10] M. Nicklas, M. Brando, G. Knebel, F. Mayr, W. Trinkl, and A. Loidl, Phys. Rev. Lett. **82**, 4268 (1999).
 - [11] S. Friedemann, N. Oeschler, S. Wirth, C. Krellner, C. Geibel, F. Steglich, S. Paschen, S. Kirchner, and Q. Si, Proc. Natl. Acad. Sci. U.S.A. **107**, 14547 (2010).
 - [12] M. C. Aronson, R. Osborn, R. A. Robinson, J. W. Lynn, R. Chau, C. L. Seaman, and M. B. Maple, Phys. Rev. Lett. **75**, 725 (1995).
 - [13] P. Coleman, Nature materials **11**, 185 (2012).
 - [14] Q. Si, S. Rabello, K. Ingersent, and J. L. Smith, Nature **413**, 804 (2001).
 - [15] P. Gegenwart, Q. Si, and F. Steglich, Nature Physics **4**, 186 (2008).
 - [16] S. Paschen, T. Lühmann, S. Wirth, P. Gegenwart, O. Trovarelli, C. Geibel, F. Steglich, P. Coleman, and Q. Si, Nature **432**, 881 (2004).
 - [17] L. Jiao, Y. Chen, Y. Kohama, D. Graf, E. D. Bauer, J. Singleton, J.-X. Zhu, Z. Weng, G. Pang, T. Shang, J. Zhang, H.-O. Lee, T. Park, M. Jaime, J. D. Thompson, F. Steglich,

- Q. Si, and H. Q. Yuan, *Proc. Natl. Acad. Sci. U.S.A.* **112**, 673 (2015).
- [18] P. Coleman, C. Pépin, Q. Si, and R. Ramazashvili, *J. Phys. Condens. Matter* **13**, R723 (2001).
- [19] A. Schröder, G. Aeppli, R. Coldea, M. Adams, O. Stockert, H. Löhneysen, E. Bucher, R. Ramazashvili, and P. Coleman, *Nature* **407**, 351 (2000).
- [20] H. Löhneysen, H. Bartolf, S. Drotziger, C. Pfleiderer, O. Stockert, D. Souptel, W. Löser, and G. Behr, *Journal of Alloys and Compounds* **408-412**, 9 (2006).
- [21] A. Schröder, G. Aeppli, E. Bucher, R. Ramazashvili, and P. Coleman, *Phys. Rev. Lett.* **80**, 5623 (1998).
- [22] H. Löhneysen, O. Stockert, and M. Enderle, *Journal of Magnetism and Magnetic Materials* **310**, 822 (2007).
- [23] O. Stockert, H. Löhneysen, A. Rosch, N. Pyka, and M. Loewenhaupt, *Physica B: Condensed Matter* **259-261**, 376 (1999).
- [24] O. Stockert, H. v. Löhneysen, W. Schmidt, M. Enderle, and M. Loewenhaupt, *J. of Low Temp. Phys.* **161**, 55 (2010).
- [25] H. Löhneysen, A. Schröder, and O. Stockert, *Solid State Commun.* **303-304**, 480 (2000).
- [26] K. Grube, W. H. Fietz, U. Tutsch, O. Stockert, and H. v. Löhneysen, *Phys. Rev. B* **60**, 11947 (1999).
- [27] R. Robinson, D. Goossens, M. Torikachvili, K. Kakurai, and H. Okumura, *Physica B: Condensed Matter* **385-386, Part 1**, 38 (2006).
- [28] M. Vrtis, J. Jorgensen, and D. Hinks, *Physica B+C* **136**, 489 (1986).
- [29] T. Suzuki, T. Goto, A. Tamaki, T. Fujimura, Y. Ōnuki, and T. Komatsubara, *J. Phys. Soc. Jpn.* **54**, 2367 (1985).
- [30] T. Goto, T. Suzuki, A. Tamaki, T. Fujimura, Y. Ōnuki, and T. Komatsubara, *J. Magn. Magn. Mater.* **63-64**, 309 (1987).
- [31] H. Löhneysen, A. Germann, and A. Schröder, *Physica B: Condensed Matter* **163**, 144 (1990).
- [32] G. Fraunberger, B. Andraka, J. S. Kim, U. Ahlheim, and G. R. Stewart, *Phys. Rev. B* **40**, 4735 (1989).
- [33] A. Germann, A. Nigam, J. Dutzi, A. Schröder, and H. v. Löhneysen, *Le Journal de Physique Colloques* **49**, C8 (1988).
- [34] A. K. Gangopadhyay, J. S. Schilling, E. Schubert, P. Gutsmiedl, F. Gross, and K. Andres, *Phys. Rev. B* **38**, 2603 (1988).
- [35] M. Sieck, C. Speck, M. Waffenschmidt, S. Mock, and H. Löhneysen, *Physica B: Condensed Matter* **223-224**, 325 (1996).
- [36] O. Isnard, J. Pierre, D. Fruchart, L. Romaka, and R. Skolozdra, *Solid State Commun.* **113**, 335 (1999).
- [37] E.-W. Scheidt, T. Schreiner, K. Heuser, and G. Stewart, *Physica B: Condensed Matter* **259**, 388 (1999).
- [38] K. Heuser, E.-W. Scheidt, T. Schreiner, and G. R. Stewart, *Phys. Rev. B* **57**, R4198 (1998).
- [39] R. Küchler, P. Gegenwart, K. Heuser, E.-W. Scheidt, G. R. Stewart, and F. Steglich, *Phys. Rev. Lett.* **93**, 096402 (2004).
- [40] J. Rodriguez-Carvajal, in *satellite meeting on powder diffraction of the XV congress of the IUCr*, Vol. 127 (Toulouse, France:[sn], 1990).
- [41] A. Wills, *Physica B: Condensed Matter* **276-278**, 680 (2000).
- [42] M. Ruck, G. Portisch, H. G. Schlager, M. Sieck, and H. v. Löhneysen, *Acta Crystallogr. Sect. B* **49**, 936 (1993).
- [43] A. C. Larson and D. T. Cromer, *Acta Crystallogr.* **14**, 545 (1961).
- [44] S. Mock, C. Paschke, A. Schröder, J. Sereni, M. Sieck, and H. Löhneysen, *Physica B: Condensed Matter* **199**, 39 (1994).
- [45] K. Yamada, I. Hirose, Y. Noda, Y. Endoh, Y. Ōnuki, and T. Komatsubara, *J. Phys. Soc. Jpn.* **56**, 3553 (1987).
- [46] P. Blaha, K. Schwarz, G. K. H. Madsen, D. Kvasnicka, and J. Luitz, *WIEN2K, An Augmented Plane Wave + Local Orbitals Program for Calculating Crystal Properties* (Karlheinz Schwarz, Techn. Universität Wien, Austria, 2001).
- [47] J. P. Perdew, K. Burke, and M. Ernzerhof, *Phys. Rev. Lett.* **77**, 3865 (1996).
- [48] H. Asano, M. Umino, Y. Ōnuki, T. Komatsubara, F. Izumi, and N. Watanabe, *J. Phys. Soc. Jpn.* **55**, 454 (1986), 10.1143/JPSJ.55.454.
- [49] G. R. Stewart, Z. Fisk, and M. S. Wire, *Phys. Rev. B* **30**, 482 (1984).
- [50] A. Zheludev, *ResLib 3.4* (Oak Ridge National Laboratory, 2007).
- [51] M. J. Cooper and R. Nathans, *Acta Crystallographica* **23**, 357 (1967).
- [52] J. M. Lawrence and S. M. Shapiro, *Phys. Rev. B* **22**, 4379 (1980).
- [53] A. Hamann, O. Stockert, V. Fritsch, K. Grube, A. Schneidewind, and H. v. Löhneysen, *Phys. Rev. Lett.* **110**, 096404 (2013).
- [54] H. von Löhneysen, A. Neubert, T. Pietrus, A. Schröder, O. Stockert, U. Tutsch, M. Loewenhaupt, A. Rosch, and P. Wölfe, *The European Physical Journal B – Condensed Matter and Complex Systems* **5**, 447 (1998).
- [55] O. Stockert, H. Löhneysen, A. Schröder, M. Loewenhaupt, N. Pyka, P. Gammel, and U. Yaron, *Physica B: Condensed Matter* **230-232**, 247 (1997).
- [56] H. Okumura, K. Kakurai, Y. Yoshida, Y. Ōnuki, and Y. Endoh, *J. Magn. Magn. Mater.* **177-181, Part 1**, 405 (1998).
- [57] K. Heuser, E.-W. Scheidt, T. Schreiner, and G. R. Stewart, *Phys. Rev. B* **58**, R15959 (1998).
- [58] H. Löhneysen, C. Pfleiderer, A. Schröder, and O. Stockert, *J. Phys. Chem. Solids* **63**, 2155 (2002).
- [59] O. Stockert, A. Schröder, H. Löhneysen, N. Pyka, E. Garcia-Matres, R. Kamp, S. Welzel, and M. Loewenhaupt, *Physica B: Condensed Matter* **259-261**, 383 (1999).
- [60] O. Stockert, A. Neubert, and H. Löhneysen, *Physica B: Condensed Matter* **230-232**, 250 (1997).
- [61] H. Löhneysen, M. Sieck, O. Stockert, and M. Waffenschmidt, *Physica B: Condensed Matter* **223-224**, 471 (1996).
- [62] S. K. Goh, D. A. Tompsett, P. J. Saines, H. C. Chang, T. Matsumoto, M. Imai, K. Yoshimura, and F. M. Grosche, *Phys. Rev. Lett.* **114**, 097002 (2015).
- [63] L. E. Klintberg, S. K. Goh, P. L. Alireza, P. J. Saines, D. A. Tompsett, P. W. Logg, J. Yang, B. Chen, K. Yoshimura, and F. M. Grosche, *Phys. Rev. Lett.* **109**, 237008 (2012).